Nano Research Energy

ISSN 2791-0091 (print); 2790-8119 (online)
https://doi.org/10.26599/NRE.2026.9120290

Research Article

Continuous gradient composite solid electrolyte with differentiated functions toward electrodes for high-performance lithium metal batteries

Yuxue Sun[1,2], Chunhui Ma[1], Herui Fu[1], Huiyao Zhang[1], Haiming Xie[1] (✉), and Jun Liu[1] (✉)

[1] *National & Local United Engineering Laboratory for Power Battery, Department of Chemistry, Northeast Normal University, Changchun 130024, China*

[2] *College of Chemistry and Chemical Engineering, Qiqihar University, Qiqihar 161006, China*

Received: 11 May 2026 / **Revised:** 2 September 2026 / **Accepted:** 5 September 2026 / **Published date:** 26 November 2026

ABSTRACT

In response to the development demand for lithium metal batteries (LMBs) with high energy density and high safety, this study reports a composite solid electrolyte (LPCNE) prepared from poly(vinylidene fluoride-*co*-hexafluoropropylene) (PVDF-HFP), cyclopentane-1,1-dicarbonitrile (CPDCN), and $Li_{6.4}La_3Zr_{1.4}Ta_{0.6}O_{12}$ (LLZTO). Through gravitational sedimentation, a functionally oriented continuous gradient structure forms inside LPCNE, in which the PVDF-HFP rich layer facing the cathode offers excellent oxidation resistance, while the high modulus LLZTO rich layer facing the lithium metal anode (LMA) effectively suppresses lithium dendrite growth. Such a continuous gradient structure eliminates the interfacial impedance caused by delamination between the organic and inorganic phases, achieving a smooth compositional transition. The incorporation of CPDCN as α-H free nitrile plasticizer increases the ionic conductivity of LPCNE to 0.69 mS·cm^{-1}, and the coordination of CPDCN with metal atoms on the LLZTO surface significantly reduces the concentration of free cyano groups, thereby effectively suppressing side reactions between cyano groups and lithium metal. Consequently, the Li/LPCNE/Li symmetric cell exhibits stable cycling for over 2000 h, and the $LiFePO_4$/LPCNE/Li cell delivers a discharge specific capacity of 158.3 mAh·g^{-1} at 0.2 C with 78.4% retention after 650 cycles. Moreover, LPCNE possesses a wide electrochemical stability window of 4.75 V, enabling the $LiNi_{0.6}Co_{0.2}Mn_{0.2}O_2$/LPCNE/Li cell to deliver a discharge specific capacity of 163.9 mAh·g^{-1} at 0.1 C with 70% retention after 250 cycles. This study achieves differentiated functionality by adjusting the gradient distribution of the composite solid electrolyte components, providing an innovative solution for high-performance LMBs.

KEYWORDS

continuous gradient structure, dinitrile additive, composite solid electrolyte, function-oriented design, lithium metal batteries

1 Introduction

In the context of rapid advancements in new energy technologies, developing lithium-ion batteries (LIBs) that combine high energy density with high safety has become a core objective for energy storage systems [1–5]. The lithium metal anode (LMA) possesses an exceptional theoretical specific capacity (3860 mAh·g^{-1}) and a low electrode potential (−3.04 V vs. standard hydrogen electrode), and it significantly increases the energy density when paired with high-voltage ternary cathodes [6–10]. However, conventional liquid electrolytes (LEs) are prone to oxidative decomposition at high voltage and also exhibit poor compatibility with LMA, which can easily lead to uncontrolled growth of lithium dendrites and ultimately to piercing the separator, causing internal short circuits [11–15]. In contrast, solid-state electrolytes (SSEs) eliminate flammable organic solvents and demonstrate superior thermal decomposition temperature and thermal stability [16–19]. Furthermore, SSEs can effectively suppress lithium dendrite penetration due to their high mechanical strength, thereby mitigating the risk of thermal runaway [20]. Consequently, SSEs are regarded as pivotal materials for the next-generation high-performance lithium metal batteries (LMBs).

SSEs are typically classified into inorganic solid electrolytes (ISEs), solid polymer electrolytes (SPEs), and composite solid electrolytes (CSEs) based on their composition [21–23]. ISEs exhibit high ionic conductivity at ambient temperature and robust mechanical properties, which can effectively inhibit lithium dendrite growth, but suffer from brittleness and poor solid-solid interfacial contact with electrodes [24, 25]. SPEs have advantages such as light weight, good flexibility and excellent compatibility

© The Author(s) 2027. Published by Tsinghua University Press. The articles published in this open access journal are distributed under the terms of the Creative Commons Attribution 4.0 International License (http://creativecommons.org/licenses/by/4.0/), which permits use, distribution and reproduction in any medium, provided the original work is properly cited.

Address correspondence to Jun Liu, liuj975@nenu.edu.cn; Haiming Xie, xiehm136@nenu.edu.cn

with electrodes, yet their ionic conductivity at ambient temperature remains inadequate [26–28]. Consequently, single-component SSEs struggle to meet the requirements for practical applications. To address these challenges, researchers have developed multilayer asymmetric CSEs that integrate the advantages of ISEs and SPEs [29, 30]. Multilayer asymmetric CSEs employ an oxidation-resistant electrolyte layer adjacent to the cathode to mitigate interfacial oxidation and decomposition during charge/discharge cycles, and a dense electrolyte layer with high shear modulus adjacent to the LMA to suppress lithium dendrite penetration [31, 32]. However, such architectures require complex layered preparation processes, which increase the thickness of the electrolyte membrane and introduce additional interlayer interface impedance, presenting a major barrier to their large-scale commercialization.

Recently, the gradient CSEs with continuous compositional changes have attracted widespread attention from researchers. The gradient structure arises from the significant density difference between high-density inorganic particles and low-density polymers within the mixture. During the settling process, the denser inorganic particles gradually sediment under gravity, while the lighter polymer floats upward, thereby forming a continuous gradient with increasing inorganic particle concentration and decreasing polymer concentration from top to bottom [33]. The strategy utilizes the differences in inherent material properties to achieve a continuous gradient transition between different electrolyte layers, thereby eliminating additional interfacial impedance. For instance, Chen et al. [23] mixed poly(ethylene glycol) diacrylate (PEGDA), bis(trifluoromethane)sulfonimide lithium (LiTFSI)/1-methyl-1-propylpyrrolidinium bis(trifluoromethanesulfonyl)imide ([Py13][TFSI]) and $Li_{6.4}La_3Zr_{1.4}Ta_{0.6}O_{12}$ (LLZTO), and used gravitational settling to form a gradient CSE and added PEGDA/succinonitrile (SN) solution dropwise on the LLZTO-poor side after UV curing for secondary curing. The resulting gradient CSE exhibits high LLZTO content on one side with superior oxidation resistance, while the opposite side features low LLZTO content and a small modulus for uniform lithium-ion (Li^+) deposition. Nevertheless, such gradient CSEs often rely on the addition of carbonate-based LEs or SN as a "soft contact" layer between the electrode and electrolyte. Although the amount of carbonate-based LEs added is minimal, their flammability still poses safety risks to LMBs. Additionally, the cyano groups (C≡N) in SN exhibit poor reductive stability with lithium metal, and its active α-hydrogen (α-H) atoms can further degrade the cycling stability of LMBs through parasitic reactions [34].

In this study, a gradient CSE (designated as LPCNE) was prepared by gravity settling, using poly(vinylidene fluoride-*co*-hexafluoropropylene) (PVDF-HFP) as the polymer matrix, cyclopentane-1,1-dicarbonitrile (CPDCN) as a novel nitrile-based plasticizer, and LLZTO as the inorganic filler. LPCNE achieves functionally oriented compartmentalization, with an LLZTO-rich bottom layer facing the LMA, which has a high mechanical modulus that can effectively suppress lithium dendrite growth, while the upper layer facing the cathode is primarily composed of PVDF-HFP, leveraging its wide electrochemical window to provide LPCNE with excellent oxidative stability. The introduced CPDCN plasticizer enhances the ionic conductivity while chelating the transition metal ions in the cathode to prevent their dissolution. Moreover, CPDCN lacks active α-H, and the N atoms in CPDCN can coordinate with La atoms in LLZTO, successfully immobilizing CPDCN in the LLZTO-rich layer, thereby eliminating parasitic side reactions between lithium metal and CPDCN. We have conducted a literature survey and compiled a comparative table (Table S1 in the Electronic Supplementary Material (ESM)) summarizing the interfacial impedance values of representative double-layer and gradient-structured electrolytes reported in recent studies. As shown in Table S1 in the ESM, our LPCNE exhibits lower interfacial impedance than these comparable systems, indicating that the continuous gradient structure eliminates interlayer interfaces in traditional layered electrolytes, effectively reducing interfacial impedance, and enables the Li/LPCNE/Li symmetric cell to achieve stable lithium deposition and stripping for over 2000 h at 0.1 $mA·cm^{-2}$. The assembled $LiFePO_4$ (LFP)/LPCNE/Li cell delivers a discharge specific capacity of 158.3 $mAh·g^{-1}$ at 0.2 C and retains 78.4% of its capacity after 650 cycles. The $LiNi_{0.6}Co_{0.2}Mn_{0.2}O_2$ (NCM622)/LPCNE/Li cell exhibits a high initial discharge specific capacity of 163.9 $mAh·g^{-1}$ at 0.1 C, with a capacity retention rate of 70% after 250 cycles. In addition, LPCNE demonstrates flame-retardant properties. The gradient CSE designed in this study provides an innovative solution for high-safety and high-voltage LMBs through precise spatial regulation of composition and function.

2 Results and discussion

2.1 The structural characteristics of LPCNE

The LPCNE membrane exhibits excellent self-supporting properties and mechanical flexibility (Fig. 1(a)), enabling it to form close contact with the electrode materials and effectively accommodate the volume changes of the electrodes during cycling. It is worth noting that the two sides of the LPCNE membrane (denoted as LPCNE_A and LPCNE_B) exhibit different colors, which may be attributed to the non-uniform distribution of composition across the two sides. To investigate the compositional distribution within the LPCNE, X-ray diffraction (XRD) analysis was performed on both sides of the LPCNE membrane. As shown in Fig. 1(b), the LPCNE_A side exhibits characteristic diffraction peaks of PVDF-HFP and LLZTO, while the LPCNE_B side primarily shows the characteristic peaks of LLZTO. Scanning electron microscopy (SEM) further confirmed the significant structural differences between the two sides. The LPCNE_A side presents a typical porous network structure of the PVDF-HFP matrix formed by solvent evaporation (Fig. 1(c)), while the LPCNE_B side clearly shows a dense layer formed by the close packing of LLZTO particles (Fig. 1(d)). Consistent with the morphological observation, the corresponding energy dispersive spectroscopy (EDS) mapping shows a higher signal intensity of lanthanum (La), zirconium (Zr) and tantalum (Ta) elements on the LPCNE_B side compared to that on the LPCNE_A side, confirming the enrichment of LLZTO in the lower layer. Cross-sectional SEM and EDS mapping of the LPCNE membrane also confirms that the LLZTO concentration gradually increases from the top to the bottom of the membrane (Fig. 1(e) and Fig. S2 in the ESM). The above analytical characterization reveals a gradient distribution of components within the LPCNE membrane, which is primarily attributed to the significant density difference between PVDF-HFP and LLZTO. The higher-density LLZTO particles settle under gravitational force and gradually accumulate in the bottom layer, while the relatively lower-density PVDF-HFP tends to float upwards, ultimately forming a continuous gradient structure (Fig. 1(f)). The PVDF-HFP-rich LPCNE_A is oriented towards the cathode in

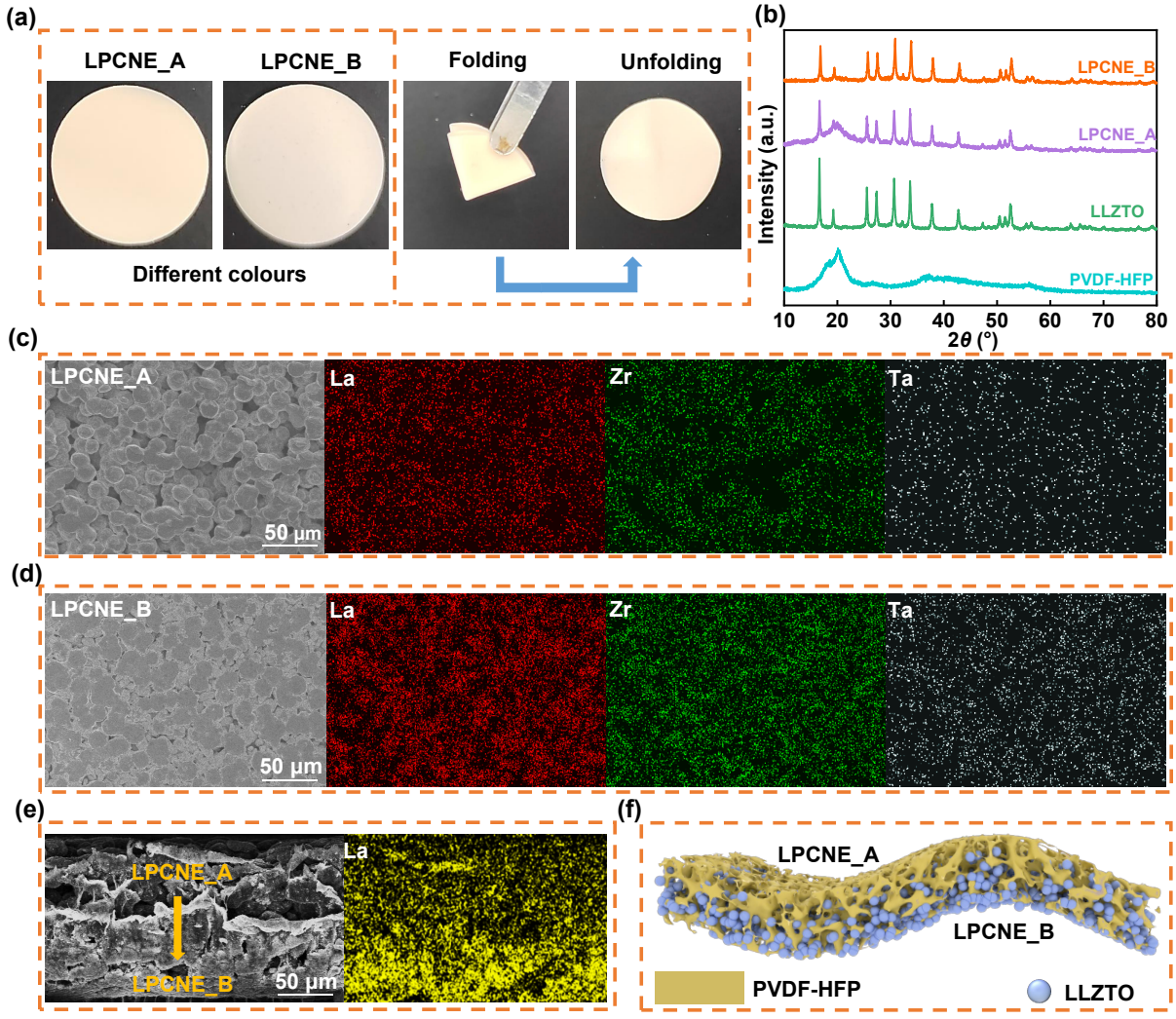


Figure 1 (a) The optical photographs of the LPCNE membranes, and its folded and unfolded images. (b) The XRD patterns of PVDF-HFP, LLZTO and LPCNE. The SEM images and EDS-mapping of (c) LPCNE_A, (d) LPCNE_B. (e) Cross-sectional SEM and EDS mapping of the LPCNE membrane. (f) Schematic diagram of the LPCNE.

LMBs, where its excellent electrochemical stability can resist oxidative decomposition. The LLZTO-rich LPCNE_B is oriented towards the LMA, where its high mechanical modulus can effectively suppress the growth and puncture of lithium dendrites during cycling, thereby enhancing the safety of LMBs.

2.2 Surface coordination interaction between LLZTO and CPDCN

To conduct a preliminary assessment of the interaction between LLZTO and CPDCN, LLZTO was immersed in CPDCN for 48 h and subsequently characterized by XRD. As shown in Fig. 2(a), the characteristic diffraction peaks of LLZTO do not shift, nor do any new diffraction peaks appear compared with the diffraction patterns of the original LLZTO, indicating that no chemical reaction occurs between LLZTO and CPDCN that can alter the bulk crystal structure of LLZTO or generate significant crystalline by-products [35]. It can therefore be inferred that the interaction between LLZTO and CPDCN is likely confined to the surface region of the LLZTO nanoparticles. To further elucidate the nature of the surface interactions, Fourier transform infrared (FTIR) spectroscopy was performed on pure CPDCN and on a mixture of CPDCN and LLZTO. As shown in Fig. 2(b), the characteristic absorption peak attributed to the cyano (C≡N) bond in pure CPDCN is located at 2250 cm^{-1}, whereas the intensity of this peak is significantly reduced after mixing with LLZTO. The reduction in intensity is attributed to the lone pair of electrons in the C≡N bond coordinating with exposed metal sites on the LLZTO surface. Such coordination results in a transfer of the electron cloud from the C≡N bond to the metal ions, thereby weakening the bond strength of the C≡N bond, which manifests as a decrease in infrared absorption intensity [36]. To further verify the above coordination mechanism, the samples were analyzed using X-ray photoelectron spectroscopy (XPS). The results show that in the mixture of CPDCN and LLZTO, the binding energy of the La 3d electrons increases compared to that of the pristine LLZTO, as evidenced by a significant shift of the characteristic XPS peak towards higher binding energies (Fig. 2(c)), confirming the existence of a coordination interaction between the C≡N groups and the La atoms on the LLZTO surface [37].

The coordination interaction between CPDCN and LLZTO offers a key advantage for the construction of a stable CSE. Firstly, the interaction effectively anchors CPDCN to the LLZTO surface, significantly reducing the concentration of free CPDCN at the LMA interface and thereby suppressing the side reaction between the C≡N groups and lithium metal at the source. More

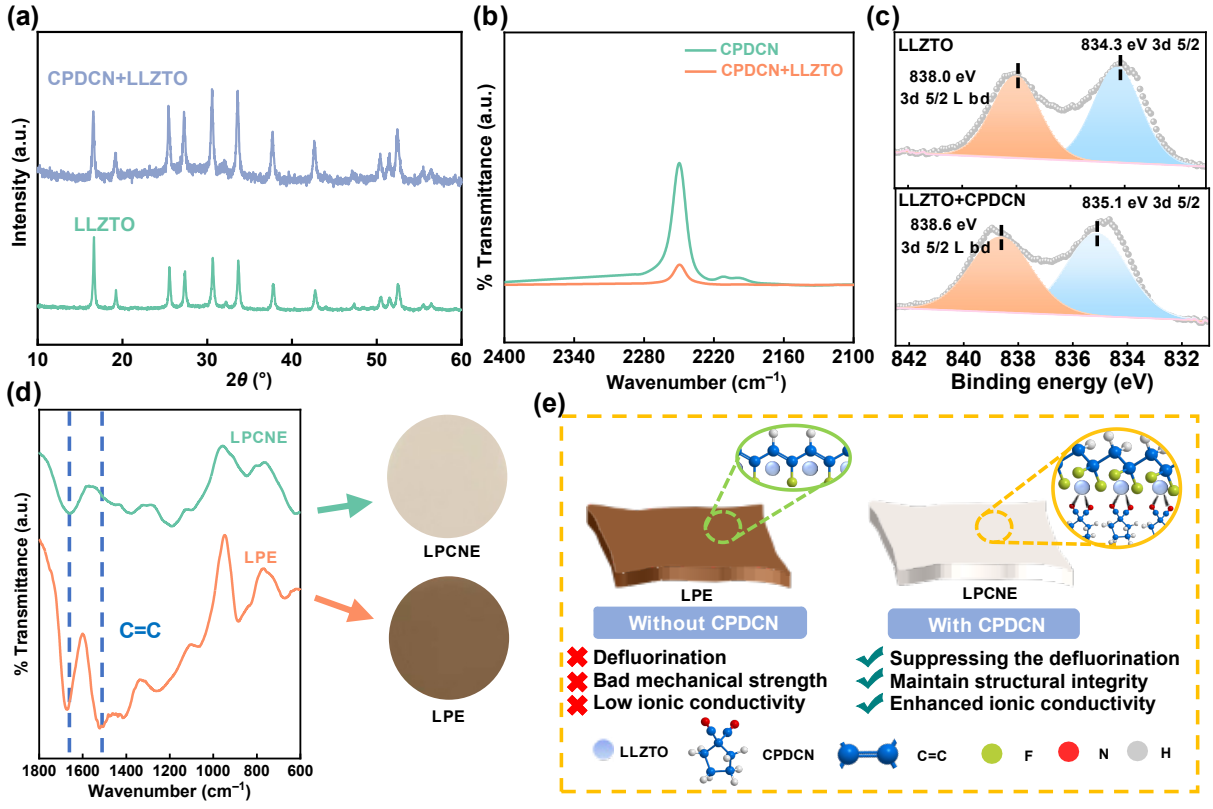


Figure 2 (a) XRD pattern of pure LLZTO and the mixture of LLZTO and CPDCN. (b) FTIR spectra of CPDCN and the mixture of LLZTO and CPDCN. (c) XPS spectra of pure LLZTO and the mixture of LLZTO and CPDCN. (d) FTIR spectra and optical photographs of LPE and LPCNE membranes. (e) Schematic illustration of the suppressing defluorination reaction.

importantly, CPDCN passivates the Lewis acidic sites on the LLZTO surface, effectively suppressing their catalytic defluorination of PVDF-HFP. The efficacy of the passivation can be visually assessed by the color of the electrolyte membrane [38]. As shown in Fig. 2(d), the LPE membrane without CPDCN exhibits a typical brown color, resulting from defluorination of PVDF-HFP induced by LLZTO to form double bonds, whereas the LPCNE membrane containing CPDCN appears pale yellow. Furthermore, the FTIR of LPE exhibits two sharp absorption peaks at 1508 cm^{-1} and 1673 cm^{-1}, corresponding to the C=C bond and the associated cross-linking products, respectively. In contrast, the 1508 cm^{-1} peak disappears in the LPCNE spectrum, and the intensity of the 1673 cm^{-1} peak is significantly reduced, indicating that the defluorination reaction is effectively suppressed (Fig. 2(e)) [39]. Furthermore, the unsaturated C=C bonds generated by defluorination exhibit a low oxidation potential, making them incompatible with high-voltage cathode materials. The reduced flexibility of PVDF molecular chains also compromises the thermal stability and mechanical strength of the CPE [40].

2.3 Li^+ transfer mechanism

To investigate the effect of component composition on ionic conductivity, five LPCNE samples with different compositions were prepared and labelled as LPCNE_X_Y_Z, where *X*, *Y* and *Z* represent the mass ratios of LLZTO, PVDF-HFP and CPDCN, respectively. As shown in Fig. 3(a), LPCNE_5_10_10 exhibits the highest ionic conductivity at ambient temperature, reaching 0.69 mS·cm^{-1}, which is significantly higher than that of the other samples. It is observed that the ionic conductivity is positively correlated with the content of CPDCN and LLZTO, which can be attributed to the synergistic formation of a continuous ionic transport network by these two components. On the one hand, LLZTO itself possesses high ionic conductivity, providing a high-speed ion transport pathway for Li^+ [41–45]. On the other hand, CPDCN utilizes its highly polar C≡N groups to form [Li^+···C≡N] coordination structures with Li^+, thereby promoting the dissociation of lithium salts and increasing the concentration of free Li^+ [46]. Consequently, Li^+ can not only migrate at high speeds within the LLZTO-rich phase but also migrate through the CPDCN-filled pores in the PVDF-HFP-rich layer. Both transmission pathways are interconnected, forming a continuous and mutually permeable ionic transport network that enables LPCNE to achieve exceptional ionic conductivity.

In order to investigate the ion transport properties and temperature dependence, the ionic conductivity of LPCNEs was measured in the temperature range of 0 to 120 °C. As shown in Fig. 3(b), the ionic conductivity of all samples closely follows the Arrhenius equation, confirming the thermally activated characteristics of ion conduction. The activation energy (E_a) value obtained through linear fitting reveals that LPCNE_5_10_10 exhibits the lowest value (0.23 eV) among all samples, indicating superior Li^+ transport kinetics and the lowest ion migration energy barrier (Fig. 3(c)). This result is consistent with its highest ionic conductivity at ambient temperature (0.69 mS·cm^{-1}), thereby supporting the ion transport mechanism described previously.

The lithium-ion transference number (t_{Li^+}) measured by chronoamperometry (CA) indicates that LPCNE_5_10_10 exhibits the highest value (0.36), which is highly consistent with the previous ionic conductivity and E_a results (Fig. 3(d) and Fig. S3 in the ESM). A higher t_{Li^+} indicates superior selectivity for Li^+ transport in LPCNE_5_10_10. The enhancement stems from the spatial confinement of anion migration imposed by the LLZTO

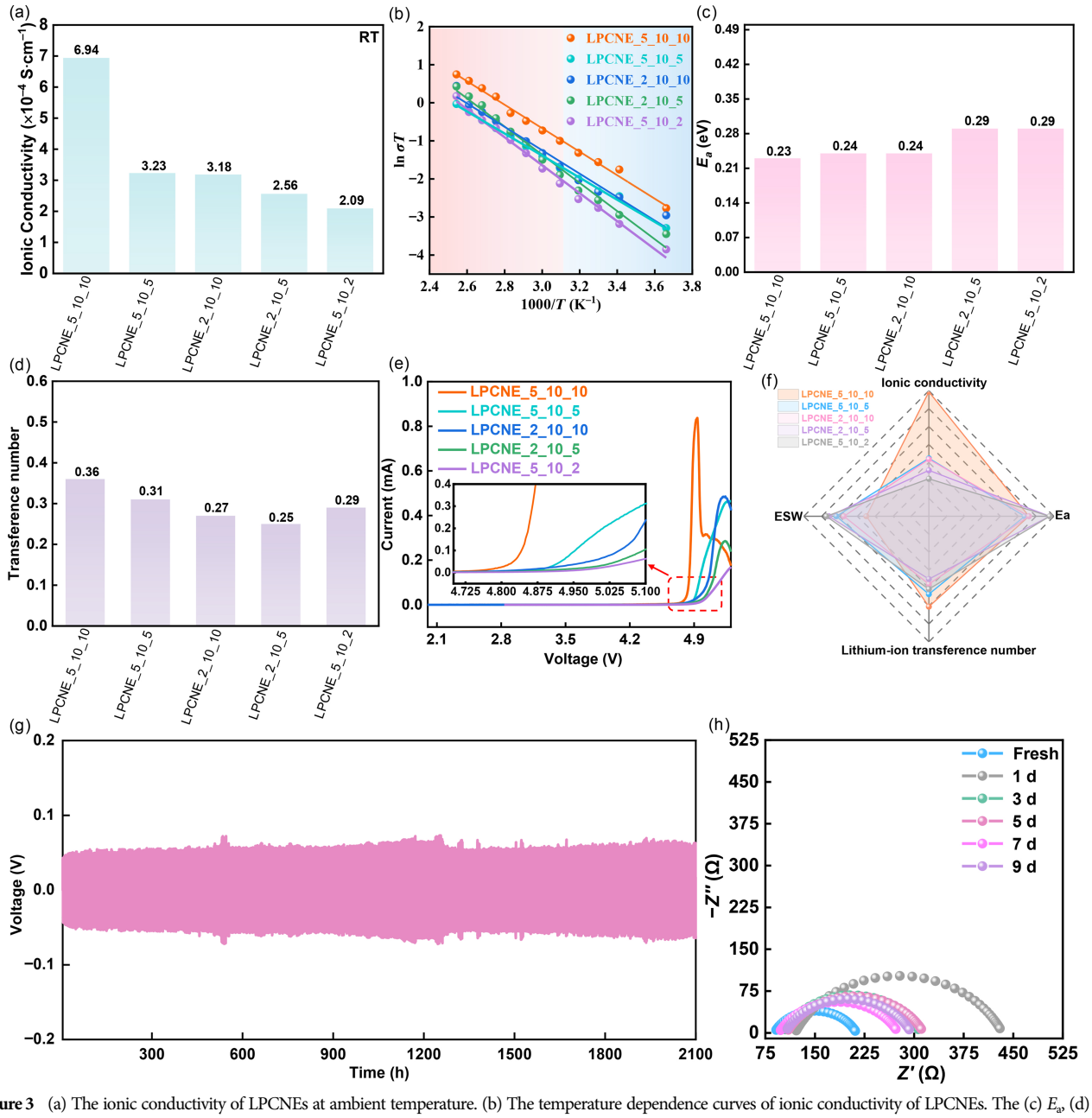


Figure 3 (a) The ionic conductivity of LPCNEs at ambient temperature. (b) The temperature dependence curves of ionic conductivity of LPCNEs. The (c) E_a, (d) t_{Li^+} and (e) LSV curves of LPCNEs. (f) Comparison graph of the comprehensive properties of LPCNEs. (g) The constant-current plating/stripping curve of Li/LPCNE/Li cell. (h) The EIS plots of the Li/LPCNE/Li cell for different placement time.

lattice structure, while the C≡N groups in CPDCN coordinate with Li^+, promoting lithium salt dissociation and increasing the concentration of free Li^+. The electrochemical stability of LPCNE was evaluated via linear sweep voltammetry (LSV). As shown in Fig. 3(e), the onset potential for oxidation of LPCNE_5_10_10 (4.75 V) is slightly lower than that of other samples. Nevertheless, its electrochemical stability window (ESW) fully meets the voltage range required for high-voltage LMBs in practical applications. Furthermore, a radar plot was employed to comprehensively evaluate multiple key performance indicators. As shown in Fig. 3(f), LPCNE_5_10_10 exhibits balanced and excellent performance across various dimensions, including ionic conductivity, E_a, t_{Li^+} and ESW. Based on the above comprehensive comparison, LPCNE_5_10_10 is ultimately selected as the optimal composition for subsequent battery performance evaluation.

To evaluate the interfacial compatibility between LPCNE and LMA, a Li/LPCNE/Li symmetric cell was assembled and subjected to constant-current plating/stripping tests. As shown in Fig. 3(g), the cell exhibits highly stable cycling performance over 2000 h while maintaining a low overpotential of 0.06 V. The stability is primarily attributed to the high ionic conductivity and high ionic mobility of LPCNE, which effectively mitigate polarization within the cell. To further verify LPCNE's ability to inhibit lithium dendrite growth, we have performed additional galvanostatic cycling tests on Li/LPCNE/Li symmetric cells at a higher current density of 1 mA·cm^{-2}. As presented in Fig. S4 in the ESM, the cell delivers stable plating/stripping performance for over 200 h with a low and stable overpotential, without any sign of short-circuit. This result clearly confirms that the LPCNE membrane, with its LLZTO-rich bottom layer, can effectively suppress lithium dendrite growth even under a practically relevant current density. Subsequently, electrochemical impedance spectroscopy (EIS) was

employed to dynamically monitor the interfacial charge transfer process. As shown in Fig. 3(h), with increasing cell stand time, the interfacial impedance first increases and then decreases, and eventually stabilizes at approximately 180 Ω after 9 days. The trend indicates the formation of a stable and dense solid electrolyte interphase (SEI) layer on the LMA surface. To clarify the contribution of the LLZTO filler to the mechanical properties of LPCNE, a control sample (PCNE) without LLZTO was prepared using the same fabrication process as LPCNE, and tensile tests were conducted on both samples. According to the stress-strain curves (Fig. S5 in the ESM), the maximum tensile strength of PCNE is 11.2 MPa, whereas that of LPCNE is significantly increased to 14.6 MPa. The results confirm that the incorporation of LLZTO not only enhances the mechanical strength of LPCNE but also increases the mechanical modulus through the enrichment of LLZTO on the LMA side, thereby physically blocking the penetration and propagation of dendrites [47].

2.4 The performance of LMBs based on LPCNE

LMBs were assembled using LPCNE, and their electrochemical performance was evaluated at ambient temperature. When LFP is used as the cathode material, the cell achieves a maximum discharge specific capacity of 158.3 mAh·g^{-1} at 0.2 C, with a capacity retention rate as high as 78.4% after 650 cycles (Fig. 4(a)). For the NCM622 cathode, the cell achieves a maximum discharge specific capacity of 163.9 mAh·g^{-1} at 0.1 C, with a capacity retention of 70% after 250 cycles (Fig. 4(c)). Furthermore, when using the high-nickel cathode material $LiNi_{0.8}Co_{0.1}Mn_{0.1}O_2$ (NCM811), the cell exhibits a maximum discharge specific capacity of 199.6 mAh·g^{-1} at a 0.1 C rate, and retains 94.2% of its capacity after 57 cycles (Fig. 4(e)). These results clearly demonstrate that LMBs using LPCNE possess excellent long-term cycling stability. To further verify the durability and practical applicability of LPCNE, we have prepared LFP cathodes with a mass loading of 7.912 mg·cm^{-2} and assembled LFP/LPCNE/Li cells

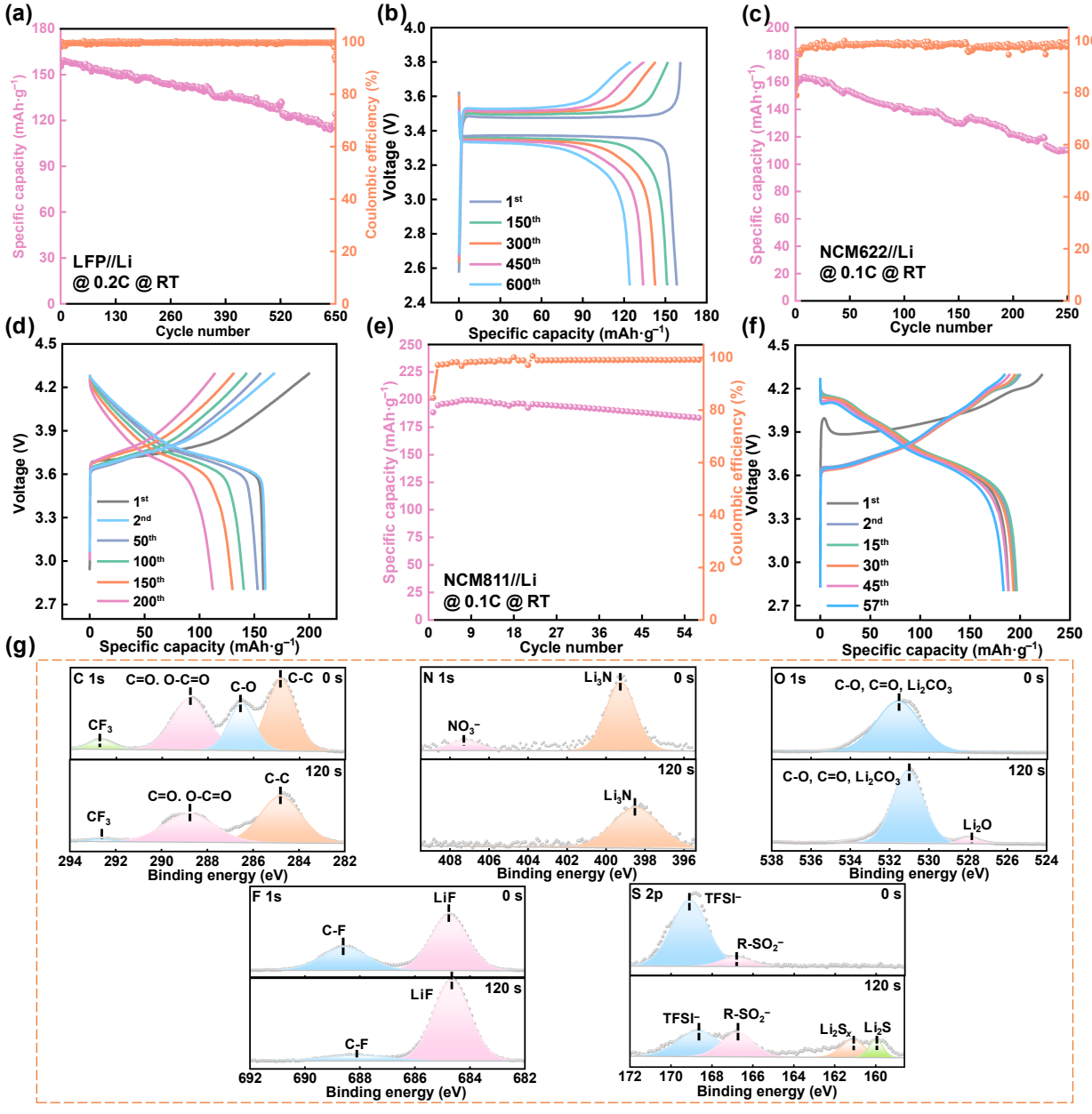


Figure 4 The long-term cycling performance of (a) LFP//Li, (c) NCM622//Li and (e) NCM811//Li cells. The corresponding charge/discharge voltage profiles of (b) LFP//Li, (d) NCM622//Li and (f) NCM811//Li cells. (g) XPS etching spectra of LMA surface after cycling of NCM622//Li cell.

for testing. As shown in Fig. S6 in the ESM, the cell delivers a specific discharge capacity of 157.5 mAh·g^{-1} at 0.1 C, and after 20 cycles, the capacity retention reaches 95.2%. This preliminary result indicates that LPCNE can maintain good interfacial stability and ionic transport capability even under high mass-loading conditions.

To analyze the composition and structure of the SEI in LMBs after cycling, SEM and X-ray photoelectron spectroscopy (XPS) were employed to characterize the surface of the LMA. For the SEM result of LMA (Fig. S7(a) in the ESM), the surface of the LMA remains smooth and flat, with no observable dendritic or mossy lithium deposits. This uniform morphology indicates the formation of a dense and homogeneous SEI layer on the LMA surface, which effectively regulates lithium deposition and suppresses parasitic side reactions. As shown in Fig. 4(g), the SEI exhibits a bilayer structure. The inner layer consists primarily of inorganic components such as LiF and Li_3N. These inorganic compounds confer high mechanical strength and elastic modulus to the inner layer, thereby effectively preventing the penetration of lithium dendrites [48]. At the same time, the inner layer possesses high lithium-ion conductivity, which facilitates the uniform diffusion and deposition of Li^+ on the electrode surface, minimizing the irreversible loss of active lithium [49]. The outer layer, on the other hand, consists mainly of organic lithium salts, which impart flexibility to the SEI, allowing it to accommodate the volume changes during lithium deposition and deintercalation, thereby preventing SEI cracking induced by stress accumulation. It is precisely the balanced and coordinated bilayer structure that ensures the structural integrity and functional stability of the SEI during long-term cycling [50]. Furthermore, XPS characterization results indicate that no characteristic C≡N peaks are detected in either the C 1s or N 1s spectra, demonstrating that CPDCN is anchored to the LLZTO surface via coordinate bonds. Consequently, side reactions between free C≡N groups and lithium metal are eliminated, significantly enhancing the chemical stability of the interface.

As shown in Figs. 4(b), 4(d) and 4(f), cells employing different cathode materials all exhibit stable voltage-polarization curves during cycling. Such excellent performance is primarily attributed to the high reversibility of both electrode interfaces, coupled with the ESW of the LPCNE itself, which spans as wide as 4.75 V. Through the synergistic action of these factors, the Li^+ deintercalation process at the cathode and the lithium metal deposition process at the anode consistently proceed with low and stable overpotentials. The stable electrode reaction kinetics not only effectively suppresses polarization accumulation but also significantly enhances the coulombic efficiency of the cell. Consequently, the cell is able to maintain high efficiency and stable energy output during long-term cycling.

The structural stability of cathode materials is one of the key factors determining the long-term cycling performance of cells, and the formation and composition of the cathode-electrolyte interface (CEI) have a direct impact on cathode stability [51]. To investigate the morphology and composition of the CEI, the surface of the cycled NCM622 cathode was characterized using transmission electron microscopy (TEM) and XPS. TEM analysis reveals that the cycled NCM622 cathode surface is covered by a uniform and dense CEI layer approximately 2 nm thick (Fig. 5(a)). For the SEM result of the NCM622 cathode (Fig. S7(b) in the ESM), the cathode particles retain their intact spherical morphology with no visible cracks, pulverization, or detachment from the conductive matrix. This observation demonstrates that the CEI layer formed during cycling effectively preserves the structural integrity of the cathode material.

Further XPS depth-section analysis (Figs. 5(b)–5(f)) shows that, as the etching depth increases, the organic content gradually decreases, while LiF content rises significantly. Simultaneously, Li_3N exhibits a relatively uniform distribution throughout the CEI, from the outer to the inner layers. The moderate organic content in the outer layer confers good flexibility and adaptability to the CEI, helping to alleviate the volumetric stress generated during cycling. The inwardly enriched and highly stable LiF forms a dense and robust inner barrier, effectively protecting the cathode material from electrolyte corrosion [52]. The uniformly distributed Li_3N constructs an efficient ion-conducting network throughout the CEI, ensuring rapid and uniform Li^+ transport. Furthermore, characteristic signals of the C≡N bond are observable in both the C 1s and N 1s spectra (Figs. 5(b) and 5(c)). The formation of strong coordination bonds between the C≡N bond and the transition metal ions exposed on the cathode surface effectively inhibits the dissolution of the metal ions. The CEI structure, which combines gradient stability with uniform ion transport properties, lays a crucial foundation for maintaining the structural integrity and electrochemical stability of the NCM622 cathode during long-term cycling.

The formation mechanism of the gradient-structured SEI and CEI is primarily governed by the electrode surface potential. In the region adjacent to the electrode, LiTFSI and CPDCN undergo deep decomposition to yield stable inorganic products (LiF, Li_3N, and Li_2O) which constitute the inner layer. In contrast, farther from the electrode surface, the diminished driving force for decomposition allows the polymer matrix and its derivatives to form the organic outer layer. Furthermore, the electron-withdrawing interaction between La^{3+} and the C≡N groups redirect the decomposition pathway, suppressing the direct formation of organic lithium nitrile salts and promoting the preferential generation of Li_3N. Additionally, La^{3+} on the LLZTO surface acts as a Lewis acid site, forming coordination bonds with the oxygen atoms in $TFSI^-$. This coordination facilitates $TFSI^-$ decomposition and favors cleavage of the C–S bond to produce LiF, rather than cleavage of the C–F bond, which would otherwise lead to sulfur-containing organic species.

To evaluate the practicality of LPCNEs, LFP/LPCNE_5_10_10/Li pouch cell was assembled and tested for mechanical compatibility alongside electrochemical stability. As shown in Fig. 5(g), the open-circuit voltage of the pouch cell in its initial state is 3.43 V. After two successive cuts, the cell voltage stabilizes at 3.38 V and 3.35 V, respectively, with only minor fluctuations, indicating that the cell maintains good electrochemical stability even under mechanical deformation. Furthermore, when the cell is folded to 90° and 180°, it continues to supply a stable power source to the LED light throughout the entire deformation process, further confirming the excellent mechanical compatibility of the cell. The thermal safety of LPCNEs was evaluated using thermogravimetric analysis (TGA) and flammability testing. TGA results show that LPCNEs exhibit good thermal stability during heating, with virtually no mass loss below 100 °C (Fig. S8 in the ESM). The flame-retardant behaviour of LPCNEs is further examined via flammability testing. As shown in Fig. S9 in the ESM, LPCNEs self-extinguish rapidly upon removal from an open flame, with no sustained burning observed, indicating that they possess excellent flame-retardant properties capable of effectively suppressing the combustion risk during thermal runaway, thereby significantly enhancing the overall safety of LMBs.

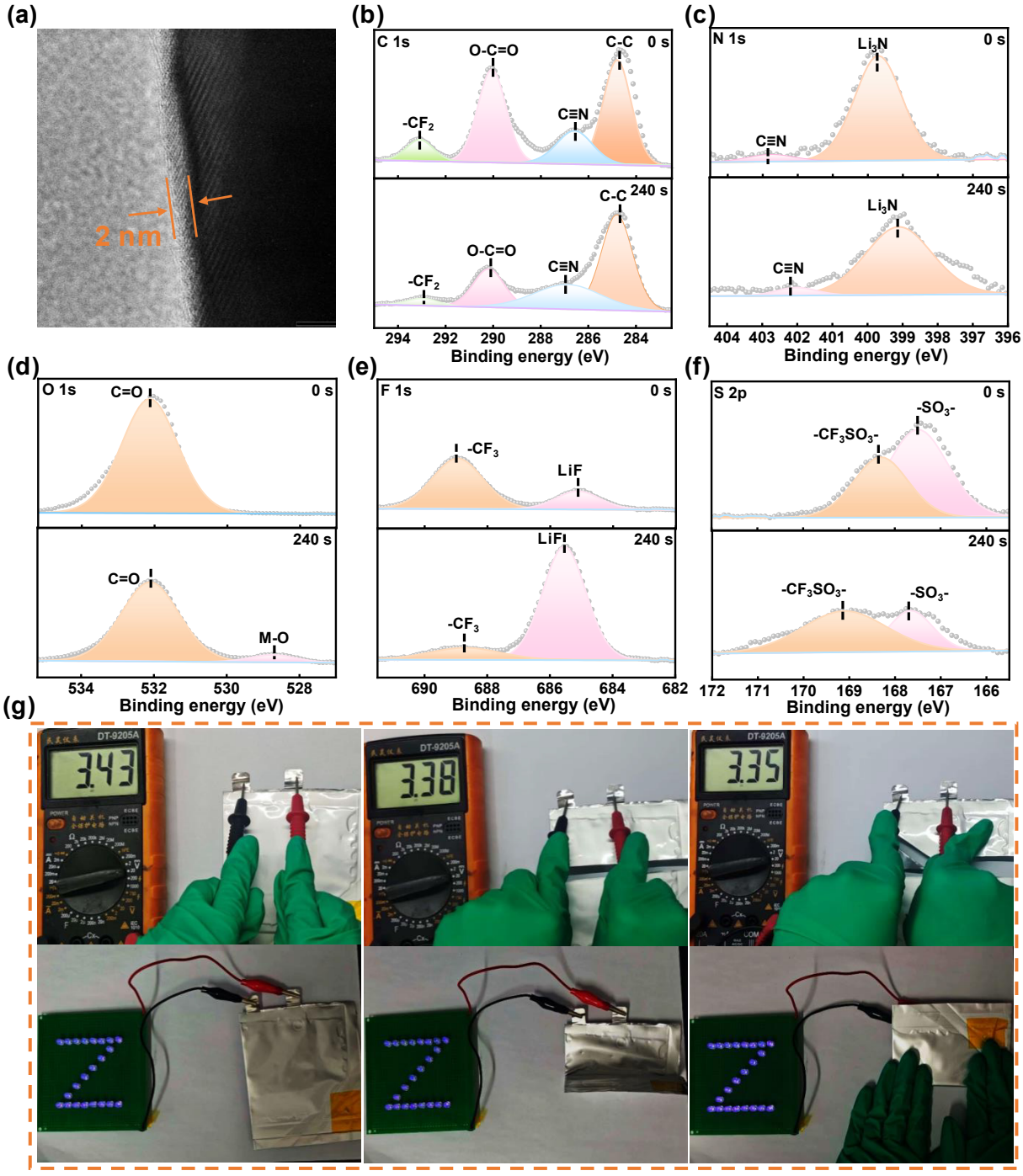


Figure 5 (a) TEM analysis of NCM622 cathode surface after cycling. XPS spectra depth analysis of cathode surface: (b) C 1s, (c) N 1s, (d) O 1s, (e) F 1s, and (f) S 2p. (g) The mechanical compatibility and electrochemical stability of LFP/LPCNE_5_10_10/Li pouch cell.

3 Conclusion

In this study, a CSE (LPCNE) with a gradient distribution of PVDF-HFP and LLZTO was successfully prepared using the gravity sedimentation method. The gradient distribution structure enables LPCNE to form functional compartments, with the region facing the cathode exhibiting antioxidant properties and the region facing the anode effectively suppressing lithium dendrite growth. Concurrently, the structure effectively eliminates the interlayer interface resistance commonly found in traditional layered electrolytes. The introduced CPDCN coordinates with the LLZTO surface, anchoring the cyano groups to the LLZTO surface. The coordination significantly reduces side reactions between free cyano groups and lithium metal, simultaneously inhibiting the catalytic degradation of the polymer matrix by LLZTO, thereby maintaining the overall structural integrity of the electrolyte membrane. Further analysis indicates that stable CEI and SEI with varying compositions have formed at the cathode and anode interfaces, respectively. The inorganic inner layer, rich in LiF and Li_3N, provides high mechanical strength and ionic conductivity, while the organic outer layer exhibits good flexibility, enabling it to accommodate volume changes in the electrodes during cycling. The synergistic interaction between the inner and outer layers significantly enhances interface stability. Owing to these properties, LPCNE exhibits high ionic conductivity and

electrochemical stability at ambient temperature. Both the Li//Li symmetric cells assembled using LPCNE and LMBs employing different cathode materials demonstrate excellent cycling stability and low polarization characteristics. The strategy of gradient distribution of electrolyte components proposed in this study provides an effective approach for the development of LMBs with high safety and high energy density.

Acknowledgements

This work was supported by Science and Technology Development Plan Project of Jilin Province (No. 20240302113GX), 2024 Capital Construction Funds within the Provincial Budget of Jilin Provincial Development and Reform Commission (2024C018-2) and the National Natural Science Foundation of China (No. 22572024).

Author contributions

Yuxue Sun: Writing-original draft, Visualization, Validation, Investigation, Formal analysis, Data curation, Conceptualization. **Chunhui Ma**: Investigation, Data curation, Software. **Herui Fu**: Investigation, Data curation, Software. **Huiyao Zhang**: Investigation, Data curation, Software. **Haiming Xie**: Conceptualization, Funding acquisition, Formal analysis, Supervision. **Jun Liu**: Conceptualization, Funding acquisition, Formal analysis, Supervision, Writing-review & editing.

Declaration of conflicting interests

The authors declare no conflicting interests regarding the content of this article.

Data availability

All data needed to support the conclusions in the paper are presented in the manuscript and/or the Supplementary Materials. Additional data related to this paper may be requested from the corresponding author upon request.

Electronic Supplementary Material: Supplementary material (material synthesis, electrode and electrolyte preparation, characterization and electrochemical testing methods, comparative data on key performance metrics, and a series of supplementary figures) is available in the online version of this article at https://doi.org/10.26599/NRE.2026.9120290.

References

[1] Armand, M.; Tarascon, J. M. Building better batteries. *Nature* **2008**, *451*, 652–657.

[2] Yu, L.; Yu, L.; Liu, Q.; Meng, T.; Wang, S.; Hu, X. L. Monolithic task-specific ionogel electrolyte membrane enables high-performance solid-state lithium-metal batteries in wide temperature range. *Adv. Funct. Mater.* **2022**, *32*, 2110653.

[3] Yin, J. Y.; Xu, X.; Jiang, S.; Wu, H. H.; Wei, L.; Li, Y. D.; He, J. P.; Xi, K.; Gao, Y. F. High ionic conductivity PEO-based electrolyte with 3D framework for dendrite-free solid-state lithium metal batteries at ambient temperature. *Chem. Eng. J.* **2022**, *431*, 133352.

[4] Xia, S. X.; Wu, X. S.; Zhang, Z. C.; Cui, Y.; Liu, W. Practical challenges and future perspectives of all-solid-state lithium-metal batteries. *Chem* **2019**, *5*, 753–785.

[5] Liu, P.; Zhang, J. W.; Zhong, L.; Huang, S.; Gong, L.; Han, D. M.; Wang, S. J.; Xiao, M.; Meng, Y. Z. Interphase building of organic-inorganic hybrid polymer solid electrolyte with uniform intermolecular Li^+ path for stable lithium metal batteries. *Small* **2021**, *17*, 2102454.

[6] Chen, X. B.; Put, B.; Sagara, A.; Gandrud, K.; Murata, M.; Steele, J. A.; Yabe, H.; Hantschel, T.; Roeffaers, M.; Tomiyama, M. et al. Silica gel solid nanocomposite electrolytes with interfacial conductivity promotion exceeding the bulk Li-ion conductivity of the ionic liquid electrolyte filler. *Sci. Adv.* **2020**, *6*, eaav3400.

[7] Yuan, H. D.; Nai, J. W.; Fang, Y. J.; Lu, G. X.; Tao, X. Y.; Lou, X. W. Double-shelled C@MoS_2 structures preloaded with sulfur: An additive reservoir for stable lithium metal anodes. *Angew. Chem., Int. Ed.* **2020**, *59*, 15839–15843.

[8] Chen, K.; Liu, J.; Zhang, X. R.; Sun, Y. X.; Xie, H. M. Three-dimensional cross-linked network deep eutectic gel polymer electrolyte with the self-healing ability enable by hydrogen bonds and dynamic disulfide bonds. *J. Colloid Interface Sci.* **2024**, *669*, 529–536.

[9] Yao, Y.; Wang, H. Y.; Yang, H.; Zeng, S. F.; Xu, R.; Liu, F. F.; Shi, P. C.; Feng, Y. Z.; Wang, K.; Yang, W. J. et al. A dual-functional conductive framework embedded with TiN-VN heterostructures for highly efficient polysulfide and lithium regulation toward stable Li–S full batteries. *Adv. Mater.* **2020**, *32*, 1905658.

[10] Li, L. S.; Deng, Y. F.; Chen, G. H. Status and prospect of garnet/polymer solid composite electrolytes for all-solid-state lithium batteries. *J. Energy Chem.* **2020**, *50*, 154–177.

[11] Jiang, Y.; Chu, X.; Li, J.; Dong, F. L.; Qiao, Q. M.; Cai, L. Z.; Liu, J.; Xie, H. M. Constructing stable interface and high-performance solid polymer electrolyte by introducing MgF_2 for dendrite-free Li metal batteries. *J. Energy Storage* **2025**, *113*, 115686.

[12] Goodenough, J. B.; Kim, Y. Challenges for rechargeable Li batteries. *Chem. Mater.* **2010**, *22*, 587–603.

[13] Guo, J.; Xu, H. L.; Sun, Y. X.; Chen, K.; Zhang, X. R.; Xie, H. M.; Jiang, Y.; Liu, J. Borate-containing triblock copolymer electrolytes for improved lithium-ion transference number and interface stability. *J. Colloid Interface Sci.* **2024**, *660*, 565–573.

[14] Li, N. W.; Yin, Y. X.; Yang, C. P.; Guo, Y. G. An artificial solid electrolyte interphase layer for stable lithium metal anodes. *Adv. Mater.* **2016**, *28*, 1853–1858.

[15] Ma, Q. Y.; Zheng, Y.; Luo, D.; Or, T.; Liu, Y. Z.; Yang, L. X.; Dou, H. Z.; Liang, J. Q.; Nie, Y. H.; Wang, X. et al. 2D materials for all-solid-state lithium batteries. *Adv. Mater.* **2022**, *34*, 2108079.

[16] Jiang, Y.; Chen, K.; He, J. P.; Sun, Y. X.; Zhang, X. R.; Yang, X. X.; Xie, H. M.; Liu, J. A self-healing composite solid electrolyte with dynamic three-dimensional inorganic/organic hybrid network for flexible all-solid-state lithium metal batteries. *J. Colloid Interface Sci.* **2025**, *678*, 200–209.

[17] Wu, Y. J.; Wang, S.; Li, H.; Chen, L. Q.; Wu, F. Progress in thermal stability of all-solid-state-Li-ion-batteries. *InfoMat* **2021**, *3*, 827–853.

[18] Han, L. F.; Wang, L.; Chen, Z. H.; Kan, Y. C.; Hu, Y.; Zhang, H.; He, X. M. Incombustible polymer electrolyte boosting safety of solid-state lithium batteries: A review. *Adv. Funct. Mater.* **2023**, *33*, 2300892.

[19] Chen, K.; Sun, Y. X.; Zhang, X. R.; Liu, J.; Xie, H. M. A self-healing and nonflammable cross-linked network polymer electrolyte with the combination of hydrogen bonds and dynamic disulfide bonds for lithium metal batteries. *Energy Environ. Mater.* **2023**, *6*, e12568.

[20] Liu, W. C.; Li, G.; Yu, W.; Gao, L.; Shi, D. J.; Ju, J. G.; Deng, N. P.; Kang, W. M. Asymmetric organic-inorganic bi-functional composite solid-state electrolyte for long stable cycling of high-voltage lithium battery. *Energy Storage Mater.* **2023**, *63*, 103005.

[21] Chen, X. Z.; He, W. J.; Ding, L. X.; Wang, S. Q.; Wang, H. H. Enhancing interfacial contact in all solid state batteries with a cathode-supported solid electrolyte membrane framework. *Energy Environ. Sci.* **2019**, *12*, 938–944.

[22] Zhang, X. R.; Liu, S. Y.; Sun, Y. X.; Gao, L. J.; Chen, K.; Dong, F. L.; Sun, H.; Xie, H. M.; Liu, J. Surface coordination of garnet fillers

improves the organic-inorganic interfacial compatibility of composite solid electrolyte. *Small* **2024**, *20*, 2405909.
[23] Deng, C. L.; Chen, N.; Hou, C. Y.; Liu, H. X.; Zhou, Z. M.; Chen, R. J. Enhancing interfacial contact in solid-state batteries with a gradient composite solid electrolyte. *Small* **2021**, *17*, 2006578.
[24] Jiang, H.; Wu, Y. Y.; Ma, J.; Liu, Y. C.; Wang, L. L.; Yao, X.; Xiang, H. F. Ultrathin polymer-in-ceramic and ceramic-in-polymer bilayer composite solid electrolyte membrane for high-voltage lithium metal batteries. *J. Membrane Sci.* **2021**, *640*, 119840.
[25] Yu, X. W.; Liu, Y. J.; Goodenough, J. B.; Manthiram, A. Rationally designed PEGDA-LLZTO composite electrolyte for solid-state lithium batteries. *ACS Appl. Mater. Interfaces* **2021**, *13*, 30703–30711.
[26] Bai, L.; Ghiassinejad, S.; Brassinne, J.; Fu, Y.; Wang, J. D.; Yang, H.; Vlad, A.; Minoia, A.; Lazzaroni, R.; Gohy, J. F. High salt-content plasticized flame-retardant polymer electrolytes. *ACS Appl. Mater. Interfaces* **2021**, *13*, 44844–44859.
[27] Li, Y. H.; Sun, Z. J.; Shi, L.; Lu, S. Y.; Sun, Z. H.; Shi, Y. C.; Wu, H.; Zhang, Y. F.; Ding, S. J. Poly (ionic liquid)-polyethylene oxide semi-interpenetrating polymer network solid electrolyte for safe lithium metal batteries. *Chem. Eng. J.* **2019**, *375*, 121925.
[28] Hu, J. L.; Chen, K. Y.; Yao, Z. G.; Li, C. L. Unlocking solid-state conversion batteries reinforced by hierarchical microsphere stacked polymer electrolyte. *Sci. Bull.* **2021**, *66*, 694–707.
[29] Yan, C. Y.; Zhu, P.; Jia, H.; Du, Z.; Zhu, J. D.; Orenstein, R.; Cheng, H.; Wu, N. Q.; Dirican, M.; Zhang, X. W. Garnet-rich composite solid electrolytes for dendrite-free, high-rate, solid-state lithium-metal batteries. *Energy Storage Mater.* **2020**, *26*, 448–456.
[30] Pan, K. C.; Zhang, L.; Qian, W. W.; Wu, X. K.; Dong, K.; Zhang, H. T.; Zhang, S. J. A flexible ceramic/polymer hybrid solid electrolyte for solid-state lithium metal batteries. *Adv. Mater.* **2020**, *32*, 2000399.
[31] Jiang, B. W.; Wei, Y.; Wu, J. Y.; Cheng, H.; Yuan, L. X.; Li, Z.; Xu, H. H.; Huang, Y. H. Recent progress of asymmetric solid-state electrolytes for lithium/sodium-metal batteries. *EnergyChem* **2021**, *3*, 100058.
[32] Zhang, Z.; Gou, J. R.; Cui, K. X.; Zhang, X.; Yao, Y. J.; Wang, S. Q.; Wang, H. H. 12. 6 μm-thick asymmetric composite electrolyte with superior interfacial stability for solid-state lithium-metal batteries. *Nano-Micro Lett.* **2024**, *16*, 181.
[33] Wu, J. Y.; Ju, Z. Y.; Zhang, X.; Marschilok, A. C.; Takeuchi, K. J.; Wang, H. L.; Takeuchi, E. S.; Yu, G. H. Gradient design for high-energy and high-power batteries. *Adv. Mater.* **2022**, *34*, 2202780.
[34] Zhang, J. N.; Wu, H.; Du, X. F.; Zhang, H.; Huang, L.; Sun, F.; Liu, T. T.; Tian, S. W.; Zhou, L. X.; Hu, S. J. et al. Smart deep eutectic electrolyte enabling thermally induced shutdown toward high-safety lithium metal batteries. *Adv. Energy Mater.* **2023**, *13*, 2202529.
[35] Fu, F.; Liu, Y.; Sun, C.; Cong, L. N.; Liu, Y. L.; Sun, L. Q.; Xie, H. M. Unveiling and alleviating chemical "crosstalk" of succinonitrile molecules in hierarchical electrolyte for high-voltage solid-state lithium metal batteries. *Energy Environ. Mater.* **2023**, *6*, e12367.
[36] Zhang, X.; Liu, T.; Zhang, S. F.; Huang, X.; Xu, B. Q.; Lin, Y. H.; Xu, B.; Li, L. L.; Nan, C. W.; Shen, Y. Synergistic coupling between $Li_{6.75}La_3Zr_{1.75}Ta_{0.25}O_{12}$ and poly (vinylidene fluoride) induces high ionic conductivity, mechanical strength, and thermal stability of solid composite electrolytes. *J. Am. Chem. Soc.* **2017**, *139*, 13779–13785.
[37] Shang, Y. N.; Xu, X.; Gao, B. Y.; Yue, Q. Y. Highly selective and efficient removal of fluoride from aqueous solution by Zr–La dual-metal hydroxide anchored bio-sorbents. *J. Clean. Prod.* **2018**, *199*, 36–46.
[38] Zhang, Q. Q.; Liu, K.; Ding, F.; Li, W.; Liu, X. J.; Zhang, J. L. Enhancing the high voltage interface compatibility of $LiNi_{0.5}Co_{0.2}Mn_{0.3}O_2$ in the succinonitrile-based electrolyte. *Electrochim. Acta* **2019**, *298*, 818–826.
[39] Zhang, S. C.; Shen, J.; Qiu, X. P.; Weng, D. S.; Zhu, W. T. ESR and vibrational spectroscopy study on poly (vinylidene fluoride) membranes with alkaline treatment. *J. Power Sources* **2006**, *153*, 234–238.
[40] Yi, X. R.; Guo, Y.; Chi, S. J.; Pan, S. Y.; Geng, C. N.; Li, M. Y.; Li, Z. S.; Lv, W.; Wu, S. C.; Yang, Q. H. Surface Li_2CO_3 mediated phosphorization enables compatible interfaces of composite polymer electrolyte for solid-state lithium batteries. *Adv. Funct. Mater.* **2023**, *33*, 2303574.
[41] Qin, Z. W.; Xie, Y. M.; Meng, X. C.; Qian, D. L.; Shan, C.; Mao, D. X.; He, G.; Zheng, Z.; Wan, L.; Huang, Y. X. Interface engineering for garnet-type electrolyte enables low interfacial resistance in solid-state lithium batteries. *Chem. Eng. J.* **2022**, *447*, 137538.
[42] Wu, J. L.; Chen, W. H.; Hao, B.; Jiang, Z. J.; Jin, G. R.; Jiang, Z. Q. Garnet-type solid-state electrolytes: Crystal-phase regulation and interface modification for enhanced lithium metal batteries. *Small* **2025**, *21*, 2407983.
[43] Chu, J. W.; Li, Z. W.; Wang, J.; Huang, G.; Zhang, X. B. Optimization strategies for key interfaces of LLZO-based solid-state lithium metal batteries. *Mater. Chem. Front.* **2024**, *8*, 2109–2134.
[44] Huang, Z. Y.; Chen, L. H.; Huang, B.; Xu, B. Y.; Shao, G.; Wang, H. L.; Li, Y. T.; Wang, C. A. Enhanced performance of $Li_{6.4}La_3Zr_{1.4}Ta_{0.6}O_{12}$ solid electrolyte by the regulation of grain and grain boundary phases. *ACS Appl. Mater. Interfaces* **2020**, *12*, 56118–56125.
[45] Wu, J. L.; Chen, W. H.; Hao, B.; Wang, Y. C.; Xu, Z. J.; Wang, Q. S.; Jiang, Z. J.; Jiang, Z. Q. Deciphering solid-state battery interface failure: Plasma-assisted bulk-interface lithium diffusion kinetics regulation. *Adv. Funct. Mater.* **2026**, *36*, e21740.
[46] Sun, Y. X.; Wang, M.; Zhang, X. R.; Xie, H. M.; Liu, J. Additive-free nitrile-based gel polymer electrolytes with enhanced interfacial compatibility for Lithium metal batteries. *Chem. Eng. J.* **2025**, *519*, 165528.
[47] Zhang, X. Y.; Wang, A. X.; Liu, X. J.; Luo, J. Y. Dendrites in lithium metal anodes: Suppression, regulation, and elimination. *Acc. Chem. Res.* **2019**, *52*, 3223–3232.
[48] Hao, C. Y.; Guo, W.; Zhao, G. Q.; Zhang, X. M.; Wang, Y.; Liu, J. B.; Zhang, X.; Zhang, X. Y.; Gao, M. X.; Pan, H. G. et al. Li_3N-enriched solid electrolyte interphase derived from interfacial catalysis toward high-performance lithium metal batteries. *Adv. Mater.* **2026**, *38*, e72588.
[49] Liu, S. J.; Shen, X. L.; Wei, L. Y.; Wang, R.; Ding, B.; Yu, J. Y.; Yan, J. H. Molecular coordination induced high ionic conductivity of composite electrolytes and stable LiF/Li_3N interface in long-term cycling all-solid-state lithium metal batteries. *Energy Storage Mater.* **2023**, *59*, 102773.
[50] Wang, Q.; Yang, J.; Huang, X. Y.; Zhai, Z. H.; Tang, J. X.; You, J. H.; Shi, C. G.; Li, W. Z.; Dai, P.; Zheng, W. C. et al. Rigid and flexible SEI layer formed over a cross-linked polymer for enhanced ultrathin Li metal anode performance. *Adv. Energy Mater.* **2022**, *12*, 2103972.
[51] Ren, J. C.; Zhu, H.; Fang, Y. J.; Li, W. B.; Lan, S.; Wei, S. C.; Yin, Z. J.; Tang, Y.; Ren, Y.; Liu, Q. Typical cathode materials for lithium-ion and sodium-ion batteries: From structural design to performance optimization. *Carbon Neutralization* **2023**, *2*, 339–377.
[52] Liu, Q.; Sun, Y. J.; Wang, S. M.; An, Q.; Duan, L. Y.; Zhao, G. F.; Wang, C. H.; Doyle-Davis, K.; Guo, H.; Sun, X. L. Highly adaptable SEI/CEI interfacial layers enabling remarkable performance of high-nickel solid-state batteries. *Mater. Today* **2023**, *64*, 21–30.



Yuxue Sun earned her Ph.D. from the School of Chemistry at Northeast Normal University in 2026. During her doctoral studies, she was also a member of the National & Local United Engineering Laboratory for Power Battery. She is currently a faculty member in the School of Chemistry and Chemical Engineering at Qiqihar University. During her Ph.D. studies, her primary research focus was on solid-state electrolytes for lithium-metal batteries, with a particular emphasis on the application of novel nitrile-based additives.



Chunhui Ma is a doctoral student at the School of Chemistry and the National & Local United Engineering Laboratory for Power Battery at Northeast Normal University, where she is pursuing her Ph.D. under the supervision of Professor Liu Jun. Her primary research focuses on the preparation of asymmetric ether-based electrolytes and their application in high-voltage lithium metal batteries.



Herui Fu is a master candidate in the Department of Chemistry, Northeast Normal University, National & Local United Engineering Laboratory for Power Battery. Working in the group of Liu Jun, he is engaged in the development of self-healing polymer-based solid-state electrolytes for lithium-metal batteries.



Huiyao Zhang is a master's student in the Department of Chemistry, Northeast Normal University, and National & Local United Engineering Laboratory for Power Battery. She pursues her master's degree under the supervision of Jun Liu. Her research concentrates on self-healing gel and solid electrolytes for lithium metal batteries.



Haiming Xie is a professor of Department of Chemistry at the Northeast Normal University and the director of National & Local United Engineering Laboratory for Power Battery. He received his Ph.D. degree from Northeast Normal University in 2008. His main research interests include lithium iron phosphate cathode materials and heat-resistant separators for high safety and high-power lithium-ion batteries, low-temperature power batteries and all-solid-state electrolytes for lithium batteries.



Jun Liu received his bachelor's degree in 2002 at the Department of Chemistry, Northeast Normal University, China. After obtaining his Ph.D. in 2007 at the same university, Jun Liu spent one year as a postdoctoral fellow with Prof. Petri Pihko at the University of Jyvaskyla, Finland. Currently he is working at Northeast Normal University, where his research interests involve solid-state electrolytes and high-voltage liquid electrolytes for lithium batteries.